Purifying single photon emission from a CdSe/CdS colloidal quantum dot

Sergii Morozov,[1] Stefano Vezzoli,[2] Alina Myslovska,[3] Alessio Di Giacomo,[3]
N. Asger Mortensen,[1, 4] Iwan Moreels,[3] and Riccardo Sapienza[2]

[1]*Center for Nano Optics, University of Southern Denmark, Campusvej 55, DK-5230 Odense M, Denmark*
[2]*The Blackett Laboratory, Department of Physics,*
Imperial College London, London SW7 2BW, United Kingdom
[3]*Department of Chemistry, Ghent University, Krijgslaan 281-S3, Gent 9000, Belgium*
[4]*Danish Institute for Advanced Study, University of Southern Denmark, Campusvej 55, DK-5230 Odense M, Denmark*
(Dated: November 19, 2021)

Colloidal quantum dots are robust and flexible single photon emitters for room-temperature applications, but their purity is strongly reduced at high pump powers, due to multiexcitonic emission which cannot be easily filtered due to the photo-luminescence spectral broadening at room temperature. Giant-shell quantum dots feature a large blueshift of the biexciton spectrum due to electron-hole wave function engineering and piezoelectric charge separation, which can be exploited for spectral separation of the single exciton from the multiexciton emission. Here, by spectral filtering, we show that we can recover an excellent single-photon emission, with $g_2(0) < 0.05$ (resolution limited), even at high pump powers above saturation of the exciton emission. The bright and pure single-photon generation shown here has important applications in quantum information technology and random-number generation.

INTRODUCTION

Colloidal quantum dots have great potential for room-temperature single-photon emitters with widely tunable optical properties. The electron and hole wave functions and the resulting exciton emission wavelength and quantum properties can be designed by the quantum dot shape and morphology [1, 2]. Giant core-shell hetero-nanocrystals reduce Auger recombination and protect the excitons from surface interactions, therefore reducing blinking and increasing photo-stability [3, 4]. Moreover, stable neutral multiexcitons with blueshifted emission energies can be formed in giant-shell quantum dots [5–7]. Giant-shell wurtzite nanocrystals provide an additional toolset to tune the spectral separation of neutral and multi excitons through the strain-induced piezoelectric field [7, 8].

Blink-free, robust and pure photon emission from colloidal quantum dots is significant for quantum applications, where bright deterministic single-photon sources are required. However, their omnidirectional radiation pattern and efficient multiexciton emission limit their application so far [9, 10]. Plasmonic and dielectric antennas can provide both efficient photon extraction [11, 12] and can increase the quantum dot brightness via the Purcell effect [13], albeit also promoting the multiexciton formation via the large light field enhancement, and therefore reducing the photon purity. The common strategy of reducing the multiexciton contribution, by reducing the excitation below saturation [14], is not entirely effective and it limits drastically the single-photon brightness [15] and the ability to produce photons on demand.

Common techniques to remove the multiexciton contribution from the signal while keeping high brightness are temporal, polarization and spectral filtering. By tem-poral filtering, photons with a fast decay time can be removed after time-tagging their arrival time at the detector, and the second-order correlation function $g_2(0)$ of colloidal quantum dot emission filtered with this method has been measured to be less than 0.01 at room temperature [16]. However, the temporal filtering is based on post-processing of the acquired data, thus it is not suitable for all applications [17]; moreover, this technique inevitably filters some of the exciton radiation, especially when the exciton is in charged states with short lifetimes. Polarization and spectral filtering of unwanted multiexciton contributions is so far restricted to cryogenic quantum emitters, as these techniques are inefficient at room temperature due to the significantly broadened emission lines and polarization decoherence [18]. Spectral filtering at room temperature can suppress the background signal during antibunching measurements [19], while also
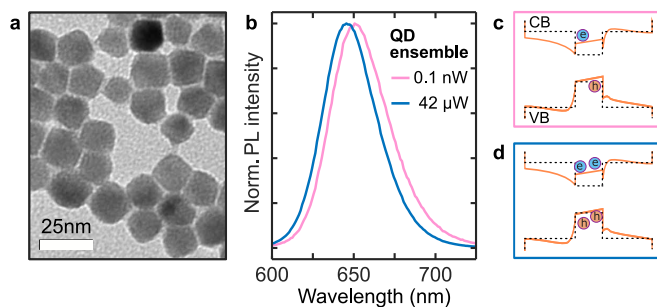

FIG. 1: **Giant-shell CdSe/CdS colloidal quantum dots with a large biexciton blueshift. a** TEM image of quantum dots with a 3.4 nm CdSe core and a thick shell consisting of ca. 20 CdS monolayers. **b** Photoluminescence spectra of quantum dot ensemble demonstrate a blueshift at high excitation power. **c-d** Schematics explaining the biexciton blueshift (see text).

providing a tool for the separation of high-order multi-excitons using the asymmetric Hanbury Brown and Twiss (HBT) interferometer [5].

In this Letter, we show that strain-induced piezo-electric effects at the core-shell interface in giant-shell CdSe/CdS quantum dots offer a large multiexciton blueshift of 25 ± 3 nm. We exploit this large blueshift to spectrally separate the single and multi photon emission in an individual quantum dot. We demonstrate a single-photon purity of $g_2(0) < 0.1$ at saturation excitation while keeping a high average brightness $(0.27 \pm 0.03) \times 10^6$ photons/s.

RESULTS AND DISCUSSION

Blueshift of multiexciton emission

We synthesized colloidal CdSe/CdS core/shell quantum dots following a protocol reported in [20] with a modification (see Methods). The quantum dots have a 3.4 nm CdSe core covered by a thick shell consisting of 20 CdS monolayers, resulting in a total diameter of 17 ± 3 nm (Fig. 1a). We used a pulsed blue laser (1 MHz, 404 nm) to excite quantum dots (see Methods). Due to the giant-shell motif, the absorption occurs preferably in the CdS shell with a consequent relaxation of carriers to the CdSe core, where radiative recombination occurs. The radiative relaxation of generated excitonic states at room temperature results in emission around 650 nm with a full-width-at-half-maximum (FWHM) of 30–60 nm (see SI Fig. S1).

The photoluminescence spectrum experiences a blueshift at high excitation power. This is demonstrated in quantum dot ensemble measurements at low and high excitation power in Fig. 1b. Fig. 1c-d schematically shows the expected band structure. As a result of strain at the interface, the bands are tilted, which in combination with the delocalization of the electron wave function results in an effective separation of electrons and holes. As a result, upon high power excitation, repulsive interactions between the holes dominate the biexciton emission energy, which lies to the blue of the exciton emission.

Photoluminescence at high pump fluency

The ability of a quantum dot to generate only one photon at a time degrades at high pump fluency due to the efficient multiexciton generation and multi-photon emission from them. Next to direct photon emission, a multiexciton can also relax to the single exciton state through Auger-assisted processes which lead to a single photon emission, but plagued with intensity and lifetime blinking [21]. Fig. 2 presents the photoluminescence response of a representative individual quantum dot (labeled QD16) to a low, $\langle N \rangle = 0.15$, and saturating, $\langle N \rangle = 1.23$, pump fluency. Here, $\langle N \rangle$ represents the mean number of electron-hole pairs generated by a laser pulse and it is proportional to the excitation power [6, 22]. We note that N follows a Poissonian distribution with average $\langle N \rangle$ and so multiple electron-hole pairs can be generated even below saturation, although a significant portion of them decay nonradiatively due to Auger recombination, which is the reason why colloidal quantum dots are single photon emitters at room temperature [6]. However, at high pump fluency and large $\langle N \rangle$, radiative recombinations from multi-excitons become increasingly more likely, degrading the purity of the source, as shown in Fig. 2c.

We excited quantum dots at 1 MHz pump rate, thus limiting the maximum output photoluminescence emission rate from a single quantum dot to 1 Mcounts/s (SI Fig. S2 and Fig. S3). The count rates reported in Fig. 2a-b are corrected for the radiation pattern of a quantum dot and the collection efficiency $\eta \sim 30\%$ of our setup [12], hence representing the absolute quantum yield, or brightness, of the emission (detected counts are about a third of those reported here). For instance, QD16 exhibits a single exciton intensity of about 0.7 ± 0.1 Mcounts/s above saturation, indicating a high single exciton quantum yield at room temperature of about 70% (see the saturation curve in SI Fig. S3b).

Further increase of pump fluency suppresses the neutral exciton emission and increases the probability of multiexciton emission, while also increasing intensity fluctuations and the likelihood of charged states [23]. For this reason, the best pump regime for source brightness is near the saturation fluency. The intensity time traces and corresponding occurrences histograms in Fig. 2a-b reveal the binary blinking and flickering at the low and high pump fluency, respectively. We also note that we used a very short binning time 10 ms in Fig. 2a-b to capture fast blinking events. We assign the intensity response at low pump fluency (Fig. 2a) to the blinking primarily between neutral and positively charged excitons [24, 25]. The flickering at high pump fluency (Fig. 2b) is arising from the emission of neutral and negatively charged excitons, which are formed when excited multi-excitons loose carriers through the Auger-driven processes.

Fig. 2c presents intensity correlation histograms $g_2(\tau)$ acquired at low and high pump fluency. We fit the histograms with an intensity autocorrelation function $g_2(\tau)$ [26], and extract the single-photon purity $g_2(0) = 0.07$ at low $(\langle N \rangle = 0.15)$ and $g_2(0) = 0.20$ at high $(\langle N \rangle = 1.23)$ pump fluency, respectively. We note that our experimental values of $g_2(0)$ are limited to about 0.05 by counting electronics in our experimental setup and avalanche photodiodes, and for more accurate $g_2(0)$ measurements one needs to use, for example, background-free superconducting nanowire single-photon detectors [16]. The fit of $g_2(\tau)$ also allows us to quantify the multi-

exciton contribution to photoluminescence emission by comparing the area of the central peak to that of a side peak in the intensity correlation histograms [5, 6]. We extract effective multiexciton contributions for QD16 of $A_{MX}^{\langle N \rangle \ll 1} = 0.5\%$ and $A_{MX}^{\langle N \rangle > 1} = 4.4\%$ out of the total photoluminescence signal at the low and high pump fluency, respectively (SI Fig. S4). In Fig. 2c, the appearance of the peak at zero correlation time at high pump fluency (blue) is the signature of multiexcitonic emission (see the evolution of the peak in SI Fig. S5).

Multi-excitons are characterized by short radiative lifetimes as the Auger-related non-radiative relaxation rate grows quadratically with the number of charges [21, 24]. The decay histograms measured at the low and saturating pump fluency (Fig. 2d) deviate from single-exponential decays and both of them contain a short and long decay components. In the low pump fluency case (pink curve), the short decay component does not originate from the multiexciton emission, as its contribution is negligible, thus we assign it to the trion emission visible in the blinking dynamics [24, 25]. At the saturating pump fluency (blue in Fig. 2d), the decay histogram has a prominent contribution at the short delay times, which is originating from the multiexciton emission and faster than that of the fundamental exciton emission.

Single photon purification using a long-pass filter at 650 nm

The biexciton emission is blue-shifted with respect to the emission of neutral and charged excitons, which we confirmed in the experiments at the ensemble level (Fig. 1b), as well as at the individual quantum dot level (SI Fig. S3a). Fig. 3 presents results on the spectral filtering of the photoluminescence spectrum of individual quantum dots. We removed part of the biexciton emission using a long-pass optical filter at 650 nm as shown in Fig. 3a,d. Fig. 3a shows the emission spectrum (blue) and its filtered part (green) of the individual QD16 from Fig. 2, when excited near saturation at $\langle N \rangle = 1.23$. Removing the blue part of emission spectrum affects drastically the photon purity and lifetime, as shown in Fig. 3b-c. The green $g_2(\tau)$ histogram in Fig. 3b is missing the multi-photon peak at zero correlation time, demonstrating that bi-excitonic emission can be effectively suppressed by spectral filtering due to the large separation of exciton and bi-exciton spectra. Fig. 3c shows the filtered decay histogram (green), where the photons at short delay times are filtered with the blue part of photoluminescence spectrum. The green decay in Fig. 3c is comparable to the one measured at low pump fluency (pink in Fig. 2d). Fitting of the filtered $g_2(\tau)$ histogram results in a single-photon purity of $g_2(0) = 0.05$, resolution limited, which is 4 times better than that of unfiltered photoluminescence signal (blue histograms in
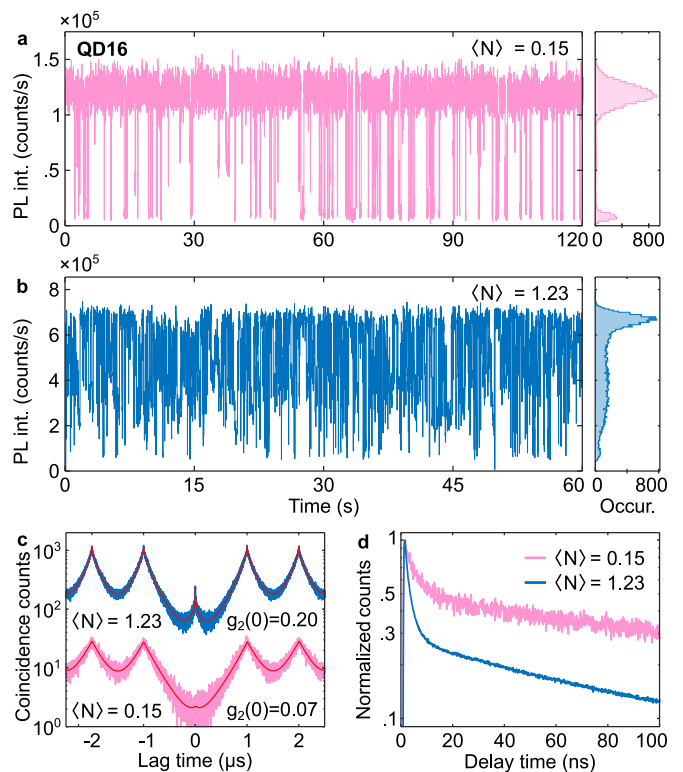

FIG. 2: **Degradation of single-photon purity at intensity saturation.** **a,b** Intensity time traces with corresponding occurrences histograms of an individual quantum dot QD16 measured at low and saturating pump fluency (10 ms time bin). **c** The antibunching histogram measured around saturation (blue) has a pronounced peak at the short correlation time and characterized by a poor value of $g_2(0) = 0.2$ in contrast to that measured at the low pump fluency $g_2(0) = 0.07$ (pink). **d** Decay histograms measured below (pink) and around (blue) the saturation demonstrate the increasing contribution of multiexciton emission with short decay times.

Fig. 2d and Fig. 3b). The effective multiexciton contribution in the filtered signal dropped to $A_{MX}^{\text{filt}} = 0.7\%$, which is comparable to that extracted at low excitation power. However, spectral filtering reduces the total photoluminescence count rate. In the case of QD16 with the emission maximum at 642 nm, the long-pass filter at 650 nm removes about 71% of photoluminescence intensity, severely compromising the brightness of the source. This clearly shows the need to search for an optimal cutoff wavelength for spectral filtering, which can balance purity with tolerable losses. This will be explored in the next section of this letter.

Fig. 3d shows another example of an individual quantum dot (labeled QD01) emitting around 669 nm, where the filtering with the long-pass filter at 650 nm cuts just 18% of its photoluminescence on the blue spectral side (see more examples in SI Fig. S6). The unfiltered correlation histogram of QD01 (blue line in Fig. 3e) was acquired at high pump fluency of $\langle N \rangle = 3.8$, which allowed for the
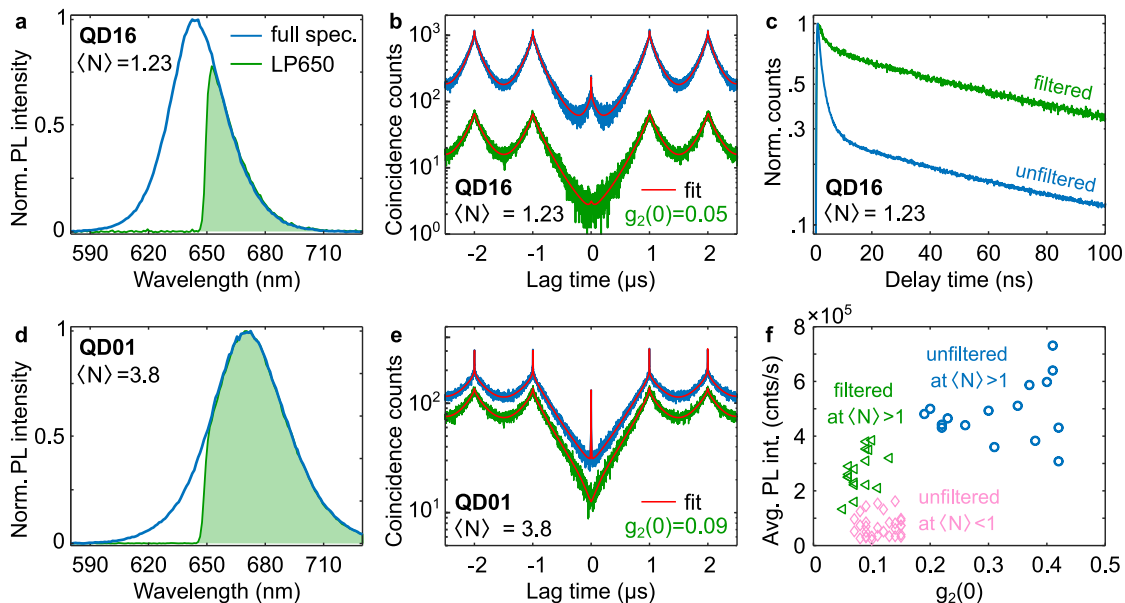
FIG. 3: Spectral filtering of an individual quantum dot emission at the saturation using a long-pass filter at 650 nm. a,d Photoluminescence spectrum of QD16 and QD01 measured at saturation (blue) and its filtered red part (green-shaded area). **b,e** The antibunching histograms of QD16 and QD01 measured at saturation pump fluency (blue) is characterized by poor, while its filtered red part does not have the characteristic peak at zero correlation times. **c** The filtered emission exhibits a decay histogram without photons with short arrival times (green), while the unfiltered emission has a strong multiexciton contribution with short decay times. **f** Single-photon purity and intensity statistics for quantum dots around saturation (blue circles), well below the saturation (pink), and filtered emission with a long-pass filter at 650 nm (green triangles).

formation of higher-order multi-excitons with enhanced recombination rates (e.g. triexciton) [5, 6]. Therefore, the unfiltered correlation histogram has additionally a sharp peak at zero correlation time and is characterized by a very poor single-photon purity $g_2(0) = 0.42$. In contrast, the sharp peak is totally removed in the filtered correlation histogram of QD01 (green line in Fig. 3e) and the single-photon purity is improved to $g_2(0) = 0.09$, again by factor of 4.7, similarly to QD16.

Due to the dot-to-dot variations typically observed within a synthesized batch, we repeated the spectral filtering experiment with a fixed cut-off at 650 nm and pump power near saturation for a number of individual quantum dots to demonstrate the improvement in single-photon purity $g_2(0)$, as function of the quantum dot brightness. Blue circles in Fig. 3f show a distribution of unfiltered intensity-$g_2(0)$ data pairs. Fig. 3f compares such distributions for filtered data at saturation (green) and that measured at low pump fluency (pink). Clearly, the green distribution shows a significant improvement in both single-photon purity $g_2(0)$ and brightness, when compared to the unfiltered distribution (pink dots). These data are summarised in Tab. 1. Note that we decided to use a single long-pass filter at fixed wavelength, and therefore, due to the variation in the emission wavelength of the quantum dots of same batch, the single photon purification is not optimal for all of them and

Pump fluency	Intensity (Mcnts/s)	$g_2(0)$
$\langle N \rangle \ll 1$	0.07 ± 0.02	0.11 ± 0.01
$\langle N \rangle > 1$, unfiltered	0.50 ± 0.05	0.34 ± 0.05
$\langle N \rangle > 1$, filtered at 650 nm	0.27 ± 0.03	0.08 ± 0.01

TABLE 1: Statistics of single photon purification using a long-pass filter at 650 nm.

could be improved.

Filtering with a tunable long-pass filter

Next we employed a tunable filter to improve the purity/brightness trade-off and assess more quantitatively the effect of spectral filtering. Fig. 4a presents a typical anti-bunching histogram acquired at high pump fluency $\langle N \rangle = 2.4$ from a quantum dot labeled QD19, obtained without spectral filtering. The fitting results in $g_2(0)$ of 0.49, as expected at the high saturation pump fluency. Using a fitting procedure (see [26] and SI Fig. S4), we decomposed the intensity contribution into the single and multiphoton emission (orange and blue shaded areas in Fig. 4a), extracting the effective multiexciton contribution $A_{MX}^{\langle N \rangle > 1} = 19\%$.

Fig. 4b shows the emission spectrum of the same QD19 measured at the same saturation pump fluency. We performed the spectral decomposition fitting (red) using 3 Voight-peak function for the biexciton, neutral, charged exciton emission, resulting in maxima respectively at 629 nm, 653 nm and 676 nm, with a biexciton emission blue-shift of 24 nm. We repeated the fit for more quantum dots to estimate the statistics of blue-shift for the ensemble to be 25 ± 3 nm (SI Fig. S7). The spectral decomposition results are shown in Fig. 4b by blue and orange shaded areas. The blue shaded area represents the biexciton emission centered at 629 nm. The orange shaded area is the sum of Voight peaks at 653 nm and 676 nm, which we assign to single photon emission originating from the neutral and charged excitons, respectively. As the feeding parameter for the blue biexciton peak intensity contribution we used the value obtained in the antibunching intensity measurement (19%). We then used the spectral decomposition to calculate how the filtering affects the intensity contribution of the biexciton in the overall signal, by relating the biexciton contribution in the photon statistics and spectral measurements.

Fig. 4c presents simulations of the expected intensity contribution from the exciton (yellow curve) and the biexciton (blue curve), as a function of the long-pass filter cut-off wavelength. The red curve represents the normalised intensity from the full spectrum, the blue and orange curves are the results of the spectral decomposition in Fig. 4b, representing single and multi photon emission, respectively. To verify the decrease of multiphoton emission (blue), we acquired photon correlation histograms with long-pass spectral filtering extracting the effective multiexciton contribution $A_{MX}^{\langle N \rangle > 1}$ (magenta points in Fig. 4c). Interestingly, we can see from this analysis that the biexciton contribution becomes almost negligible when the cut-off exceeds 660 nm, with the orange and red curve quickly converging, while the normalized intensity remains about half of the unfiltered case.

By increasing the cut-off wavelength, biexciton intensity is progressively filtered, improving the single-photon purity, with $g_2(0)$ statistics gradually improving from 0.49 to 0.08, as shown in Fig. 4d. It is obvious in this analysis that the major gain in purity, $g_2(0)$ from 0.49 to 0.22, happens with the cut-off at 633 nm, which corresponds to a minimal spectral filtering, only affecting the tail of the spectrum, thus with a very little loss (7%) of single photon emission. A cut-off at 641 nm further improves $g_2(0)$ to 0.1, while still retaining about 83% of single photon emission. This analysis shows the potential of our filtering technique in improving the single photon purity of the source without compromising its brightness.

Finally, we used the tunable long-pass filter to find the optimal cut-off wavelength. Fig. 5a presents the unfiltered antibunching histogram (blue) of a quantum dot labeled QD02, together with the filtered ones in the 621–664 nm range of the long-pass filter (colored lines). QD02
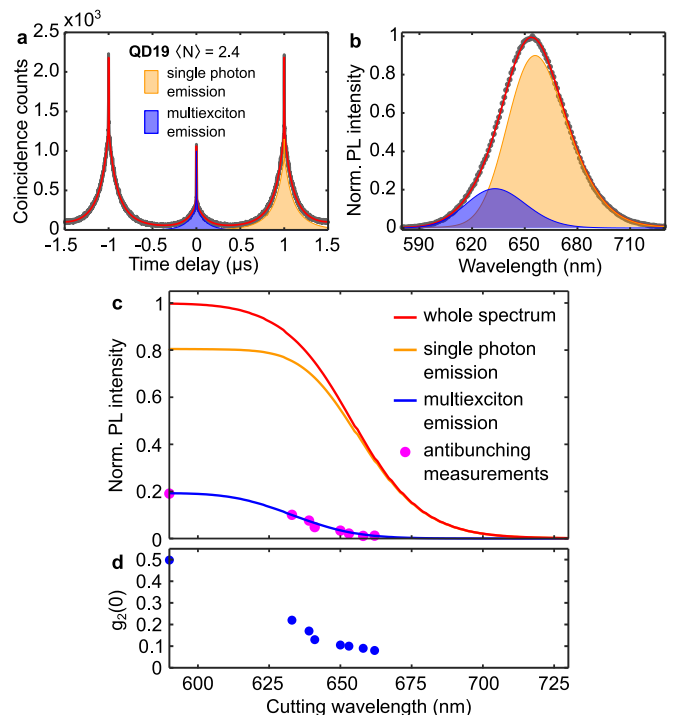

FIG. 4: **Decomposition of the photoluminescence signal into single and multiphoton emission. a** Antibunching histogram is fitted to extract the single photon (orange) and multiexciton (blue) contributions. **b** The photoluminescence spectrum acquired at the same saturation power is decomposed into peaks representing contributions of single (orange) and multi photon emission (blue). **c** Extracted from the fits in panels **a-b** intensity contributions of single (orange) and multi photon (blue) emission to the photoluminescence signal. The magenta data points were obtained from the intensity contribution analysis of corresponding antibunching histograms measured at the corresponding cutoff wavelength of the tunable filter. **d** $g_2(0)$ was extracted from antibunching histograms obtained at different tuning wavelength of the filter in the range 633–662 nm.

is here excited at high pump fluency of $\langle N \rangle = 4.2$. The unfiltered histogram (blue) has a multiexponential decay peak at zero correlation time indicating the contribution of higher-order multiexcitons at such a high pump fluency. Photoluminescence filtering in Fig. 5a with long-pass filter at 640 nm removes the fast sub-nanosecond decay component from the central peak in the autocorrelation, while further shifting the filtering wavelength above 650 nm completely removes the biexciton peak (dark red lines). We repeated this experiment for more quantum dots excited at saturation pump fluency and plot the $g_2(0)$–intensity relations in Fig. 5b (see also SI Fig. S8). The blue open symbols in Fig. 5b indicate the measured $g_2(0)$–intensity pairs of unfiltered quantum dot spectra. The tunable long-pass filter removes gradually the blue-shifted part of photoluminescence spectrum improving $g_2(0)$ and reducing the overall photoluminescence intensity resulting in the data points in Fig. 5b which
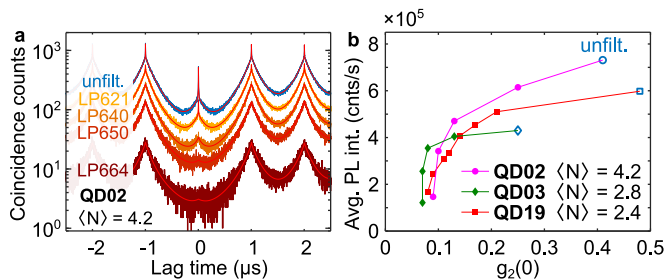
FIG. 5: Scanning photoluminescence spectrum with a tunable long pass filter. **a** Antibunching histograms of QD02 were measured at $\langle N \rangle = 4.2$ while changing the transmission of long-pass filter (see the cutting wavelength in the inset). **b** Single-photon purity $g_2(0)$ and intensity were extracted from an experiment like the one shown in panel **a**.

are connected by solid lines to help identify them. A trade-off between brightness and purity can be found by selecting the appropriate filter, depending on the sought application. Also, the lowest $g_2(0)$ value reported here is $g_2(0) = 0.05$, limited by our detection sensitivity, and is therefore only a lower bound in the $g_2(0)$ and photon purity.

CONCLUSION

In conclusion, we showed that by exploiting the piezo-electric effect in giant-shell colloidal quantum dots, which provides a large spectral separation of single and multi photon emission, we can introduce spectral filtering and improve the emission purity at room temperature. We observed a large biexciton spectral shift of $\sim 25 \pm 3$ nm, which we utilized for the spectral separation of single photon emission. We demonstrated that the spectral filtering allows to preserve single-photon purity at the saturation excitation, down to $g_2(0) = 0.05$, limited by our instrumentation, while ensuring a maximal brightness. These colloidal quantum dots are bright and pure single photon sources at room temperature, which have important applications in quantum encryption and information technologies.

MATERIALS AND METHODS

Giant-shell quantum dots.

Materials: Cadmium oxide (CdO) (99.99%, Aldrich), n-octadecylphosphonic acid (ODPA) (97%, Plasma chem), Tetradecylphosphonic acid (TDPA) (97%, Plasma chem), trioctylphosphine oxide (TOPO) (Merck), trioctylphosphine (TOP) (97%, Strem chemicals), Selenium powder (Se) (99.5%, Aldrich) and solvents: hexane, toluene, methanol (ChemLab Analytical).

Synthesis of TOP-S: A solution of 0.5 M TOP-S was prepared by dissolving 512 mg of S in 16 mL TOP and 16

mL ODE under inert atmosphere at 120 °C for 20 min. Synthesis of Cd(ol)2: 2.568 g CdO (20.06 mmol), 20 mL oleic acid and 20 mL ODE were added to a 50 mL three-necked flask. The mixture was degassed at 120 °C for 30 minutes. Degassing was followed by heating the mixture to 280 °C under inert atmosphere for CdO to dissolve and then left for 10-15 minutes at 210 °C to obtain a colorless solution. Then, the reaction mixture was again degassed for 30 min at 120 °C.

Synthesis of colloidal CdSe/CdS core/shell quantum dots: 3.4 nm CdSe core only quantum dots were synthesized analogous to the procedure in Ref. 20. The CdS shell growth procedure was performed in accordance with Ref. 27. A 50 mL three neck flask was loaded with 35 nmol of previously synthesized CdSe cores, and 10 mL ODE. The solution was degassed for 20 min at 100 °C and subsequently heated up to 280 °C. Meanwhile, in a separate vial, 2 mL 0.5 M TOP-S, 2 mL ODE, 1 mL TOP, 2 mL 0.5 M Cd(ol)2 and 1 mL of oleic acid was mixed. This solution was then injected to the solution comprising CdSe cores in the flask under nitrogen flow at a rate of 0.8 mL per hour by means of a syringe pump. When the injection was completed, the reaction was left to cool to room temperature. 25 mL of isopropanol was added in order the precipitate the quantum dots. The quantum dots were then centrifuged for 10 min at 5000 rpm. The supernatant was discarded and the precipitate redispersed in hexane.

Photoluminescence measurements. Quantum dot samples were spincoated on glass coverslips and mounted on a custom-built scanning confocal microscope. We excited quantum dots with a blue pulsed laser (LHD-P-C-405; PicoQuant) at 404 nm and 1 MHz repetition rate. An oil-immersion objective (CFI Apochromat 100×, NA=1.49; Nikon) focused a laser beam on the sample and collected generated photoluminescence. The photoluminescence signal was analyzed with a spectrometer (Kymera 193i; Andor) and in a Hanbury Brown and Twiss (HBT) interferometer. The HBT setup consisted of avalanche photo diodes (APD, SPCM-AQRH-14-TR, Excelitas Technologies) and a time-correlated single photon counting unit (Time Tagger 20; Swabian Instruments). The spectral filtering was performed using a fixed-wavelength long-pass filter at 650 nm (FELH0650, Thorlabs) and a tunable long-pass filter (TLP01-704, Semrock).

[1] C. B. Murray, C. R. Kagan, and M. G. Bawendi, Annual Review of Materials Science **30**, 545 (2000).

[2] R. E. Bailey and S. Nie, Journal of the American Chemical Society **125**, 7100 (2003).

[3] Y. Chen, J. Vela, H. Htoon, J. L. Casson, D. J. Werder, D. A. Bussian, V. I. Klimov, and J. A. Hollingsworth, Journal of the American Chemical Society **130**, 5026

(2008).

[4] W. K. Bae, L. A. Padilha, Y.-S. Park, H. McDaniel, I. Robel, J. M. Pietryga, and V. I. Klimov, ACS Nano **7**, 3411 (2013).

[5] B. Fisher, J. M. Caruge, D. Zehnder, and M. Bawendi, Physical Review Letters **94**, 087403 (2005).

[6] Y.-S. Park, A. V. Malko, J. Vela, Y. Chen, Y. Ghosh, F. García-Santamaría, J. A. Hollingsworth, V. I. Klimov, and H. Htoon, Physical Review Letters **106**, 187401 (2011).

[7] A. Polovitsyn, A. H. Khan, I. Angeloni, J. Q. Grim, J. Planelles, J. I. Climente, and I. Moreels, ACS Photonics **5**, 4561 (2018).

[8] M. Liu, N. Yazdani, M. Yarema, M. Jansen, V. Wood, and E. H. Sargent, Nature Electronics **4**, 548 (2021).

[9] Y.-S. Park, J. Roh, B. T. Diroll, R. D. Schaller, and V. I. Klimov, Nature Reviews Materials **6**, 382 (2021).

[10] R. Uppu, L. Midolo, X. Zhou, J. Carolan, and P. Lodahl, Nature Nanotechnology (2021), 10.1038/s41565-021-00965-6.

[11] N. Livneh, M. G. Harats, D. Istrati, H. S. Eisenberg, and R. Rapaport, Nano Letters **16**, 2527 (2016).

[12] S. Morozov, M. Gaio, S. A. Maier, and R. Sapienza, Nano Letters **18**, 3060 (2018).

[13] T. B. Hoang, G. M. Akselrod, C. Argyropoulos, J. Huang, D. R. Smith, and M. H. Mikkelsen, Nature Communications **6**, 7788 (2015).

[14] V. I. Klimov, Annual Review of Physical Chemistry **58**, 635 (2007).

[15] M. Nasilowski, P. Spinicelli, G. Patriarche, and B. Dubertret, Nano Letters **15**, 3953 (2015).

[16] T. Ihara, S. Miki, T. Yamada, T. Kaji, A. Otomo, I. Hosako, and H. Terai, Scientific Reports **9**, 15941 (2019).

[17] B. D. Mangum, Y. Ghosh, J. A. Hollingsworth, and H. Htoon, Optics Express **21**, 7419 (2013).

[18] H. Wang, Y.-M. He, T.-H. Chung, H. Hu, Y. Yu, S. Chen, X. Ding, M.-C. Chen, J. Qin, X. Yang, R.-Z. Liu, Z.-C. Duan, J.-P. Li, S. Gerhardt, K. Winkler, J. Jurkat, L.-J. Wang, N. Gregersen, Y.-H. Huo, Q. Dai, S. Yu, S. Höfling, C.-Y. Lu, and J.-W. Pan, Nature Photonics **13**, 770 (2019).

[19] S. Tamariz, G. Callsen, J. Stachurski, K. Shojiki, R. Butté, and N. Grandjean, ACS Photonics **7**, 1515 (2020).

[20] S. Christodoulou, G. Vaccaro, V. Pinchetti, F. D. Donato, J. Q. Grim, A. Casu, A. Genovese, G. Vicidomini, A. Diaspro, S. Brovelli, L. Manna, and I. Moreels, Journal of Materials Chemistry C **2**, 3439 (2014).

[21] C. Galland, Y. Ghosh, A. Steinbrück, M. Sykora, J. A. Hollingsworth, V. I. Klimov, and H. Htoon, Nature **479**, 203 (2011).

[22] J. A. Smyder, A. R. Amori, M. Y. Odoi, H. A. Stern, J. J. Peterson, and T. D. Krauss, Physical Chemistry Chemical Physics **16**, 25723 (2014).

[23] C. Galland, Y. Ghosh, A. Steinbrück, J. A. Hollingsworth, H. Htoon, and V. I. Klimov, Nature Communications **3**, 908 (2012).

[24] S. Morozov, E. L. Pensa, A. H. Khan, A. Polovitsyn, E. Cortés, S. A. Maier, S. Vezzoli, I. Moreels, and R. Sapienza, Science Advances **6**, eabb1821 (2020).

[25] Y.-S. Park, W. K. Bae, J. M. Pietryga, and V. I. Klimov, ACS Nano **8**, 7288 (2014).

[26] H. Nakajima, H. Kumano, H. Iijima, and I. Suemune, Applied Physics Letters **101**, 161107 (2012).

[27] L. Carbone, C. Nobile, M. D. Giorgi, F. D. Sala, G. Morello, P. Pompa, M. Hytch, E. Snoeck, A. Fiore, I. R. Franchini, M. Nadasan, A. F. Silvestre, L. Chiodo, S. Kudera, R. Cingolani, R. Krahne, and L. Manna, Nano Letters **7**, 2942 (2007).

SUPPORTING INFORMATION

Supporting Information is available

ACKNOWLEDGMENTS